Research Square

Preprints are preliminary reports that have not undergone peer review.
They should not be considered conclusive, used to inform clinical practice,
or referenced by the media as validated information.

High-Mobility P-Type Boron Carbon Nitride with Wafer-Scale Uniformity

Vincent Tung

vincent@g.ecc.u-tokyo.ac.jp

University of Tokyo https://orcid.org/0000-0003-3230-0932

Chien-Chih Tseng

University of Tokyo

Chang-Hsun Huang

National Taiwan University

Jui-Cheng Kao

Department of Materials Science and Engineering, National Yang Ming Chiao Tung University, Hsinchu 30010, Taiwan https://orcid.org/0000-0002-0147-350X

Ryo Ishikawa

University of Tokyo https://orcid.org/0000-0001-5801-0971

Seong Rae Cho

The University of Tokyo

Chengxi Lei

The University of Tokyo

Wei-Chun Chen

National Center for Instrumentation Research https://orcid.org/0000-0002-0731-418X

Ming-Chung Wu

Chang Gung University https://orcid.org/0000-0002-3584-3871

Fong-Zhi Chen

National institute of Applied Research https://orcid.org/0000-0002-2046-1715

Yu-Chieh Lo

Department of Materials Science and Engineering, National Yang Ming Chiao Tung University, Hsinchu 30010, Taiwan https://orcid.org/0000-0002-7117-9154

Ya-Lun Ho

National Institute for Materials Science https://orcid.org/0000-0001-8274-5978

Yi-Chia Chou

National Taiwan University https://orcid.org/0000-0002-7775-2927

Jui-Han Fu

The University of Tokyo

C.W. Pao

Academia Sinica https://orcid.org/0000-0003-0821-7856

Aowen Li

The University of Tokyo

Chih-Zong Deng

National Institute for Materials Science

Naoya Shibata

University of Tokyo https://orcid.org/0000-0003-3548-5952

Physical Sciences - Article

Keywords:

Posted Date: August 28th, 2025

DOI: https://doi.org/10.21203/rs.3.rs-7416428/v1

License: This work is licensed under a Creative Commons Attribution 4.0 International License. Read Full License

Additional Declarations: There is **NO** Competing Interest.

Version of Record: A version of this preprint was published at Nature on September 30th, 2026. See the published version at https://doi.org/10.1038/s41586-026-11047-9.

Abstract

A long-standing bottleneck in realizing two-dimensional (2D) CMOS technology lies in the lack of high-performance p-type semiconductors. Strong electron-doping tendencies, orbital localization, and pronounced hole scattering have collectively impeded the development of stable, efficient p-type 2D materials. Here, we report the epitaxy growth of boron carbon nitride (BCN) as a high-performance p-type semiconductor. By engineering the dehydrogenation and surface reaction pathways of monomethyl ammonia borane (MMAB) and ammonia borane (AB), we overcome a critical barrier: the spatial and temporal mismatch in the delivery of B, C, and N atoms, which disrupts lattice uniformity. The result is a wafer-scale, monolayer 2D BCN with atomically substituted carbon and dimers interspersed between continuously crystallized and locally distorted boron nitride lattices, leading to a sizable bandgap of 1.90 eV. Wafer-scale arrays of p-type BCN FETs exhibit benchmark performance, with a field-effect hole mobility of 100 $cm^2 V^{-1}s^{-1}$, on-current of 0.9 $mA\mu m^{-1}$, on/off ratio of 10^8, and threshold voltage of −0.45 V, surpassing current state-of-the-art p-type 2D semiconductors. Our findings establish BCN as a scalable and stable p-type platform, bridging a critical gap in the materials palette for 3D monolithic integration of complementary electronics.

Introduction

Despite considerable progress in n-type two-dimensional (2D) semiconductors, the development of high-performance p-type 2D counterparts remains a major bottleneck[1–4]. Challenges such as strong electron doping, orbital localization, and excessive hole scattering have severely limited the number, stability, and transport performance of p-type 2D materials, preventing their practical and monolithic integration into energy-efficient 3D complementary field-effect transistors (CFETs)[5,6]. While the discovery of graphene in 2004 ignited hopes for revolutionary electronics, its lack of a bandgap remains a key limitation. This led to flourishing research on 2D transition metal dichalcogenides (TMDs), which offer tunable electronic properties and novel devices[7]. However, most TMDs exhibit n-type or ambipolar conduction due to interfacial charge impurities and structural defects, unless they are carefully engineered at the atomically thin van der Waals (vdW) gap between TMDs and metal electrodes[6], geometrically confined within the dielectric domains[8,9,] or meticulously hyperdoped by gate-driven type-III band modulation[10]. On the other end of periodic table, p-type 2D non-TMD semiconductors, including single elements (black phosphorus[11]), ternary compound (graphene-hybridized boron nitride[12]), chalcogenides (Te), and oxides (β-Bi_2O_3[13] and Se alloyed TeO_2[14]), tend to exhibit carrier mobilities 1–2 orders of magnitude lower than their n-type counterparts, coupled with poor stability and limited scalability under processing and operational conditions. These performance disparities between n-type and p-type transport properties, uniformity, scalability, stability, and a lack of industrial compatibility inherently hinder the tantalizing prospect of implementing these materials as p-type channels[15].

In this study, we propose an epitaxy growth strategy for one-atom-thick, p-type semiconducting boron carbon nitride (BCN) with wafer-scale uniformity, high mobility, and industrial compatibility. As a ternary

2D material, BCN represents a unique expansion of the hexagonal boron nitride (hBN)[16–18] and graphene families[19,20], integrating properties from both extremes of the electronic spectrum. While graphene is a semi-metal with exceptional carrier mobility, hBN is a wide bandgap insulator (5.9 eV). By introducing atomic-scale hybridization of B, N, and C, BCN is predicted to exhibit novel electronic properties that bridge this gap[12]. Notably, theoretical studies suggest that BCN could achieve p-type transport characteristics alongside high carrier mobility and direction-dependent thermal management, making it a promising p-type building block for next-generation 3D CFETs. To this end, our precursor design originates from a systematic computational investigation of conventional precursors previously employed for BCN synthesis, which often result in phase separation or poorly defined nanoscale domains[21]. By systematic computational exploration of the dehydrogenation and surface reaction pathways of these multicomponent systems, we identified a key limitation: the spatial and temporal mismatch in the delivery of B, C, and N atoms, which hinders uniform lattice formation[22]. This led us to hypothesize that a single molecular precursor containing all three constituent elements would facilitate concerted surface reactions and promote the growth of atomically substituted lattices. Guided by this insight, we designed monomethyl ammonia borane (MMAB) coupled with ammonia borane (AB) as dual precursors. Next, 2D potential energy surface (2D-PES) simulations to map out key reaction coordinates, identifying energy barriers, selectivity windows, and bifurcation points that determine the kinetics and thermodynamics of each transformation step on the substrate. This enables us to engineer the dehydrogenation and surface reaction pathways while promoting the nucleation rate in the customized chemical vapor deposition (CVD). The result is the monolayer (ML, unless otherwise stated) 2D BCN with atomically substituted C interspersed between the continuously crystallized but locally distorted BN lattices. Our multi-scale characterizations provide a deterministic structure-property-performance relationship, linking atomic-scale bonding to device-level performance in wafer-scale arrays of FETs. The results are a mobility (μ_h) of ~ 100 cm²/V-s, an on current (I_{on}) ~ 0.9 mA/μm, a threshold voltage (V_{th}) of ~ -0.45 V, and an on/off current ratio (I_{on}/I_{off}) of ~ 10^8. In addition, we demonstrate the uniform growth of ML 2D BCN on 3D patterned SiO_2/Si substrates, thus facilitating the future integration into complex device architectures.

Figure 1a illustrates the proposed growth mechanism of BCN using MMAB and AB as dual precursors on a Cu (111) surface. First-principles calculations of reaction energies of each elementary step (Supplementary Fig. 1) reveal that AB preferentially undergoes direct dehydrogenation to form surface-bound *B–N pairs. Notably, although the direct dehydrogenation pathway of MMAB exhibits the lowest overall energy change, energy decomposition analysis reveals that cleavage of the C–N bond requires less reaction energy (Supplementary Fig. 2a)[23]. This suggests that MMAB is more likely to decompose via the formation of an *H_2BNH_2 and *CH_3 intermediate pair. The *H_2BNH_2 species tends to desorb, while the remaining *CH_3 undergoes further dehydrogenation, ultimately leaving behind a surface-bound *C species (Supplementary Fig. 2b). Together, these *B–N and *C fragments coalesce into a BCN unit, which subsequently nucleates and grows into BCN flakes (L = 1–6 units in size), culminating in the formation of extended BCN domains.

Compared to other carbon-based precursors[12], MMAB follows a prolonged decomposition pathway to generate surface-adsorbed carbon, and its relatively large molecular size suppresses surface diffusion of carbon atoms. These characteristics hinder the formation of graphene domains, instead favoring the uniform incorporation of carbon into the BCN framework. **Fig. 1b** presents the calculated formation energy for BCN flakes of varying sizes (L = 1–6) on Cu (111), referenced to the chemical potential difference between the BN and C precursors and hBN and graphene. Such a formation energy can be seen as the PES. Full computational details are provided in the Supplementary Methods. The PES reveals an apparent stabilization trend with increasing BCN size. Additionally, when the chemical potential of the precursors exceeds that of hBN and graphene, the formation of BCN flakes becomes thermodynamically favored. Conversely, a lower precursor chemical potential leads to a hybridized phase composed of hybridized hBN and graphene domains. Notably, the 'X' symbols in **Fig. 1b** mark the respective chemical potential conditions of MMAB and AB, indicating that this combination thermodynamically promotes the stabilization of a BCN monolayer on Cu (111).

To further elucidate the kinetics of BCN nucleation, a 2D nucleation rate map on Cu (111) is shown in **Fig. 1c** (see also Supplementary Fig. 3 and Supplementary Methods). Based on classical nucleation theory, the results show an exponential increase in nucleation rate with rising chemical potential and temperature. While a low chemical potential equivalent to MMAB alone (μ = 0.18 eV) can facilitate BCN nucleation, the corresponding rate is several orders of magnitude lower than that achieved with an optimized MMAB: AB ratio (μ = 0.66 eV), which yields nucleation rates exceeding 10^{15} $cm^{-2}s^{-1}$. This disparity reflects the intrinsic limitation of MMAB: its pre-existing B–N–C bonds reduce the chemical potential difference between the precursors and the BCN film, thereby weakening the thermodynamic driving force for large-area monolayer BCN growth. In contrast, proper introduction of AB raises the chemical potential of the precursor pool, restoring the strong driving force that enables efficient, large-scale BCN synthesis. Fig. 1d schematically illustrates our customized CVD growth, where dual precursors of MMAB (71%) and AB (29%) were separately annealed in sub-chambers and subsequently diluted in hydrogen and argon as carrier gases (see Methods and Supplementary Fig. 4). The concentration of each reactant can be precisely modulated by mass flow controllers (MFCs) and deposition time, thus controlling the nucleation rate while maximizing the aerial coverage[24,25]. Specifically, an atomic force microscopy (AFM) image taken after initial nucleation further suggested that edge attachment of predominantly mono-oriented BCN flakes was the primary mechanism for monolayer growth (Supplementary Fig. 5). **Figure 2** summarizes our key findings through multiscale characterizations.

Even though the atomic ratio of B, C, and N can be tuned by controlling the types and fluxes of precursors, from graphene (C, 100%) to hBN (C, 0%), the formidable challenge lies in the indeterministic control of C-atom(s) incorporation (Supplementary Fig. 6)[12,22]. High-resolution scanning transmission electron microscopy (HR-STEM) enables atomic-scale imaging by scanning a focused electron beam across a thin sample and detecting scattered electrons. This technique leverages high-angle annular dark-field (HAADF) detectors to generate atomic number-dependent contrast (Z-contrast, Z is the atomic

number), where heavier atoms appear brighter. As shown in Fig. 2a, C substitution at N sites (Z = 7) yields a slightly dimmer contrast. In contrast, when a C atom (Z = 6) substitutes a B site (Z=5) in continuously crystallized hBN lattices, the affected atom shall appear brighter than neighboring B atoms because of its higher atomic number. Indeed, the exact coordination environment of each atom can be clearly and atomically resolved. Atom-by-atom analysis reveals that 16 carbon atoms are found in the N sites, while 9 are found in the B sites, as highlighted in the highlighted areas 1, 2, and 3 (Fig. 2b, Supplementary Fig. 6a). All carbon atoms are coordinated in either atomically substituted form or dimers as shown in Fig. 2b. No hybridized domains of carbon are present, thus corroborating the efficacy of simulation, precursor engineering and CVD synthesis. Note that while the overall hexagonal structure is maintained, such a heteroatom doping is accompanied by substantial lattice distortions. In parallel, a cross-sectional HR-STEM image indicates that our BCN film consists of only one layer (Fig. 2c). This growth mode bears a close resemblance to that of graphene on Cu, which also results in a single layer under similar conditions. In parallel, electron energy loss spectroscopy (EELS, Supplementary Fig. 6b) mapping reveals the distribution of carbon atoms along the cross-section of thicker BCN films (>5 layers). It's important to note that we did not detect the presence of Cu or CuO_x, ruling out possible contamination during CVD growth. Combining HR-STEM, cross-sectional HRTEM, and EELS mapping provides critical insights into the exact coordination environment.

To determine their chemical composition and bonding type, we conducted EELS via energy losses associated with ionization edges. As suggested in **Figure 3a**, BCN spectra typically exhibit K-shell edges at 185 eV (B), 276 eV (C), and 393 eV (N), respectively[26]. Well-resolved 1s→π* and broader 1s→σ* features confirm the sp^2 hybridization of all three elements, indicating the formation of a hexagonal BCN lattice on Cu (111), consistent with the HR-STEM results in Fig. 2a[27]. Complementary X-ray photoelectron spectroscopy (XPS) measurements identify the dominant bonding configurations as indicated in Figs. 3b, c. Importantly, the shape and position of the spectra of all three elements deviate from those of previously reported BC_2N, hybridized hBN, and graphene domains. Two prominent peaks of the B 1s spectrum can be resolved at 191.0 eV and 188.0 eV, respectively. Aside from the B 1s (191.0 eV) in hBN, the pronounced shoulder at 188 eV indicates the contribution of B and C. The N 1s peak at 398.3 eV, close to that of hBN (398.1 eV), with a higher-energy shoulder, suggests partial N–C bonding. B 1s and N 1s spectra support the coexistence of B–N and B–C bonds, corroborating the XPS C 1s and HR-STEM results, where mostly N atoms are substituted by C (Supplementary Figs. 7)[28].

To evaluate the structural integrity and compositional uniformity of BCN films, Raman spectroscopy was performed on samples transferred onto a 2-inch Si/SiO_2 substrate as shown in Fig. 3d. AFM thickness measurement taken across the white solid line determines the thickness of the BCN film of ~ 0.5 nm (Fig. 3e). In addition, optical microscope (OM) image and the corresponding photoluminescence (PL) mapping, featured in Fig. 3f, g, probed at 1.85 eV collectively attest to the spatial uniformity. Spectra acquired at six randomly selected locations across the film reveal four prominent features: the pronounced and broad band at 1350 cm^{-1}, broadened G band (~1588 cm^{-1}), D' band (~1620 cm^{-1}), and reduced 2D band (~2700 cm^{-1}, Fig. 3h, i). These signatures provide important information about defect

structure, doping effects, and spatial homogeneity. The appearance of the D and D' bands—both defect-activated modes—indicates substantial lattice disorder, attributable to heteroatom substitution and topological defects within the BCN lattice framework. The I_D/I_G ratio serves as an indicator for defect density, while the emergence of the D' band suggests a distinct population of point or edge-related defects.

The G band, associated with in-plane stretching of sp² carbon atoms, is both upshifted and broadened relative to pristine graphene (~1580 cm^{-1}), reflecting significant perturbations to the BCN lattice. These spectral changes are consistent with the incorporation of carbon atoms at boron and nitrogen sites, which induce local strain and modulate the electronic structure[29]. The 2D band, an overtone of the D mode, provides further information on electronic structure and thickness. In contrast to monolayer graphene, where a sharp Lorentzian peak and $I_{2D}/I_G > 2$ are typically observed, the BCN films exhibit a broadened 2D feature and a reduced intensity ratio. This deviation is not attributed to multilayer stacking since AFM confirms monolayer coverage. It may thus be due to doping-induced modifications in the band structure and phonon dispersion. Similar to PL, the Raman spectra obtained from all six positions, as well as the large-area mapping, exhibit highly consistent peak positions, shapes, and relative intensities, underscoring the spatial uniformity and low surface roughness of the BCN films (Supplementary Fig. 8). Specifically, this uniformity attests to the reproducibility of the CVD growth process.

STS/M and DOS Bandgap Determination

Figure 4a demonstrates the electronic properties of BCN grown on Cu (111) through constant-height scanning tunneling spectroscopy measurements (STS/M)[30]. By analyzing the differential conductance (dI/dV) spectrum, we identified the energy positions where electronic states first become available for electron tunneling, locating the conduction band edge at 1.20 eV and the valence band edge at -0.7 eV. These measurements directly reveal a bandgap of 1.90 eV, thus confirming the material's semiconducting nature. The resulting bandgap is slightly smaller than the one measured by PL, since STS probes the single-particle electronic bandgap by directly mapping the density of states (DOS) in real space. Nevertheless, the spectrum exhibits clear p-type behavior, where the valence band lies closer to the Fermi level than the conduction band, which supports our device-level electrical measurements (discussed in the following paragraph). Leveraging the insights gained from STS/M results, we conducted a DOS calculation to explore the electronic structure and electrical properties of BCN. The theoretical bandgap of BCN aligns well with the STS/M results, exhibiting a slightly lower bandgap of 1.92 eV (Fig. 4b). The partial charge density of the valence band maximum (VBM) and conduction band minimum (CBM) displays the delocalized charge density distribution as shown in Fig. 4c. The DOS analysis reveals that both the VBM and CBM are predominantly derived from carbon atoms, as indicated by the orange line. This conclusion is further supported by the partial charge density distribution, which shows a clear localization of electronic states around carbon sites. Together, these results underscore

that the intrinsic electrical conductivity of BCN arises primarily from the carbon atoms incorporated into the lattice.

Electrical properties of BCN p-type FETs

To assess the potential of BCN-based semiconductors for electronic device applications, we developed bottom-gate, top-contact p-type FETs to facilitate comprehensive evaluation. Notable electrical properties of our monolayer BCN films include several key characteristics: (a) excellent transport properties that outperform those of leading p-type semiconductors, including β-Bi_2O_3[13], black phosphorus (BP) nanoribbons[11], amorphous Se-alloyed TeO_2[14], BL WSe_2[9,31], ML WSe_2[32,33], ML h-TiO_2[34], (b) uniformity over large areas and (c) industrial compatibility with 3D patterned insulating substrates. We fabricated p-channel FETs featuring BCN films as channels on a 20 nm HfO_2 dielectric, with Au/Ni source and drain electrodes (0.5-nm-thick BCN FET, length L = 1 μm, width W = 5 μm), as schematically shown in **Figure 5a, b** (also see Methods and Supplementary Fig. 9). Inset features the cross-sectional HRTEM of the ML 2D BCN after depositing on HfO_2. The transfer and output characteristics are displayed in Fig. 5c, d. The BCN FETs demonstrated typical p-channel behavior, with an average μ_h of 100 cm²/V-s, an I_{on}/I_{off} of 10^8, a low V_{th} of -0.45 V, and an I_{on} of ~0.9 mA/μm at room temperature. Notably, from the output curves, good current saturation (linearity) was observed at high (low) source-drain voltage, ruling out the influence of charge defects at the contact interface[6]. In parallel, a slightly negative V_{th} ensures the device turns on reliably when the gate is pulled to ground (0 V) while the source is at a positive supply voltage (e.g., 3.3 V or 5 V). Meanwhile, FETs comprised of ML 2D BCN thin films derived from 100% MMAB and 100% AB exhibit ambipolar semiconducting and insulating behaviors, closely resembling those of CVD-grown graphene and hBN (Supplementary Fig. 10). It is worth noting that achieving high-performance p-type 2D TMD devices necessarily involves evaporating high-work-function metals onto atomically thin 2D TMDs or tailoring carrier density at the atomically thin limit while preserving an ultraclean vdW interface between the 2D TMDs and 3D metals. Nonetheless, the overall electrical properties of FETs made with BCN exceed those of the best reported properties for single-crystalline ML-/BL WSe_2-based FETs derived from exfoliated or CVD samples with p-type electrical contacts (Fig. 5e and see Supplementary Tables 1 and 2 for details).

Additionally, we compared BCN FETs with emerging non-TMD p-type semiconductors. The comparison results are presented in Fig. 5f. The hole mobility of 2D BCN compares favorably to h-TiO_2 (10 nm) and β-Bi_2O_3 (the only two p-type metal oxides characterized by a high hole mobility over 100 cm²/V-s at room temperature). Particularly, 2D BCN surpasses these non-TMD p-type semiconductors in terms of scalability, I_{on}, V_{th}, and I_{on}/I_{off}, making it a viable candidate that meets the 2028 International Roadmap for Devices and Systems challenge for core logic devices. Next, we performed statistical analyses of the I_{on}, μ_h, V_{th}, and I_{on}/I_{off} as a function of the location of BCN FET arrays on a 2-inch wafer (224 FETs across eight runs). These FETs exhibited a narrow distribution in all four categories, with a batch-to-batch variation (temporal uniformity) of less than 10% and an estimated yield of 88.9% (Fig. 5g). Since the overall performance, epitaxial growth, scalability, and uniformity are compatible with the current n-type

MoS_2 standard, combining p-type BCN with n-type MoS_2[25] is expected to produce high-performance, low-power complementary electronics, atomically thin circuits, and junction devices. Aside from the continuous uniformity on flat metallic substrates, BCN can be deposited onto 3D patterned, insulating substrates in a conformal fashion. As demonstrated in Supplementary Fig. 11, ML BCN thin films can be selectively deposited on a holey SiO_2 dielectric as opposed to a Si substrate. The compatibility with various types of topographies in tandem with the selectivity toward amorphous dielectrics could deliver a jolt to the scalable adoption of complex device architectures such as gate-all-around FETs (GAAFETs), vertical FETs, and forksheet FETs, thereby paving the way for future commercialization.

In conclusion, we have demonstrated high-performance, wafer-scale p-channel FET arrays based on BCN semiconductors, enabled by simulation-guided CVD synthesis. Through integrated multi-scale characterization—from atomic coordination and bonding configurations to nanoscale domain structures—we established a robust feedback loop between computation, synthesis, and device optimization. The resulting devices exhibit superior electrical performance compared to state-of-the-art p-type semiconductors, including 2D TMDs, non-TMDs, oxides, and black phosphorus, while offering intrinsic stability, uniformity, and industry compatibility. We thus envision BCN as a pivotal material to complete the p-type landscape.

Methods

BCN thin-film growth and characterizations

Monolayer (ML) BCN films were synthesized via a low-pressure chemical vapor deposition (LPCVD) in a three-inch furnace tube equipped with two heating zones. The deposition process involved placing a two-inch Cu (111)/sapphire substrate in the central heating zone of the main chamber. The precursors used were ammonia borane (AB, 97%, approximately 102 mg) and monomethylamine borane (MMAB, 99%, approximately 250 mg), which were loaded into two separate sub-chambers positioned upstream of the main chamber and modulated using mass flow controllers.

Initially, the furnace was evacuated to a base pressure of 5.0 Torr. Prior to BCN growth, the substrate was annealed at 1020 °C for 60 minutes under a H_2 flow of 200 standard cubic centimeters per minute (s.c.c.m.). It is noted that humidity levels are typically around 65% in summer and 20% in winter. Annealing temperature for precursors, therefore, may vary. In general, the precursor sub-chambers were heated to 100 °C for AB and 130 °C for MMAB, respectively, using heating belts, and maintained at these temperatures for 10 minutes. Once the precursors reached the desired temperatures, they were introduced into the main chamber for a duration of 30 minutes to facilitate the growth of BCN on the Cu (111)/sapphire substrates, which were placed perpendicular to the diffusion of precursor vapors. After the growth process, the sub-chamber was sealed, and the main chamber was allowed to cool naturally to room temperature under a hydrogen gas flow of 50 s.c.c.m. The AFM images were attained in the non-contact mode using a Park NX10 AFM instrument. A probe (AC160TS) with a force constant of 26 N m^{-1} was used.

HR-STEM Characterization

For the cross-sectional observation, thin TEM lamellas were prepared by an FEI Helios G4 FIB/SEM dual-beam system with a Ga-ion source, and the STEM images were taken by a JEOL NEOARM operating at 200 kV. To observe monolayer BCN in plain view, we acquired atomic-resolution HAADF STEM images using an ARM300CF (JEOL Ltd.) microscope. To minimize electron beam damage, the microscope was operated at 60 kV and the beam current was ~ 20 pA.

STS/M Characterization

STS/M measurements were performed using a commercial Omicron VT-STM system operating under ultra-high vacuum (UHV) conditions with a base pressure of 2×10^{-10} torr. Prior to spectroscopic analysis, the synthetic BCN film was thermally annealed at 500°C for 6 hours within the UHV chamber to ensure surface cleanliness. All STS/M measurements were conducted at room temperature using constant-height mode with electrochemically etched tungsten (W) tips prepared in NaOH solution to achieve atomically sharp probe geometries. The electronic band edges were determined from the onset positions in the differential conductance (d*I*/d*V*) spectra, which are proportional to the BCN's density of states. At the onset position, the tunneling current begins to increase, indicating a transition from the bandgap region into accessible electronic states within the conduction or valence bands. This onset behavior reflects the fundamental relationship between tunneling probability and the availability of electronic states at specific energies, where the sharp rise in differential conductance directly corresponds to the band edge energy.

Density Functional Theory (DFT) calculation

Vienna *Ab Initio* Simulation Package (VASP) was used to carry out the first-principles calculations based on DFT combined with the projector augmented wave (PAW) pseudopotential method. The Perdew–Burke–Ernzerhof (PBE) functional within the generalized gradient approximation (GGA) was selected to describe the exchange-correlation interaction. The cut-off energy was set to 450 eV for the plane-wave basis set. For the decomposition pathway calculation of the ammonia borane (AB) and monomethylamine borane (MMAB), the Cu (111) surface modeled by a 6 × 6 supercell containing six atomic layers was used. The Brillouin zone (BZ) was sampled with 2 × 2 × 1 *Γ*-centered *k*-point grids for the Cu supercell. A 10 × 10 Cu (111) supercell with 1 × 1 × 1 *k*-point grid was chosen for the BCN nucleation and growth calculations. All the vacuum space along the surface normal is larger than 18 Å. DFT-D3 van der Waals (vdW) correction, developed by Grimme *et al.,* was employed to conduct the structure relaxation calculation. All geometric structures were relaxed until the electronic energy was smaller than 1.0×10^{-5} eV. The special quasi-random structure (SQS) with 72 atoms was built for the BCN monolayer using the Alloy Theoretic Automated Toolkit (ATAT). The lattice constant of the BCN is 2.509 Å, which is extracted from the HR-STEM image. The density of states (DOS) was calculated using a screened hybrid functional, HSE06, of Heyd, Ernzerhof, and Scuseria.

Device fabrication and characterization

A heavily doped Si wafer (resistivity 0.001–0.009 Ω cm) with a 20 nm ALD-grown HfO_2 was used as the gate electrode and the dielectric layer. The BCN ML channels were dry transferred onto HfO_2 as channel layers. Ni/Au source and drain electrodes were first defined through UV lithography (TuoTuo Technology, Singapore) and then deposited using a thermal evaporator to complete the bottom-gate top-contact FETs. The channel length and width were 1 and 5 μm, unless stated otherwise. All FET electrical characterizations were performed using a Keysight B1500A semiconductor analyzer in a vacuum environment.

Declarations

Acknowledgments:

C.-C.T., J.-H. Fu, and V.T. are indebted to the financial support from the Japan Society for the Promotion of Science (JSPS, 23H00253 and 24K21233), and JST, CREST Grant Number JPMJCR24A3. W.-C. Chen and F.-Z. Chen acknowledged the support from NSTC 113-2119-M-492-001-MBK and NSTC 114-2622-E-492-001. V.T. acknowledges the equipment support from TuoTuo Technology (lithography) and Enli-Technology (Probe station). J.C.K. and C.W.P. thank the support from the Academia Sinica Investigator Award (Grant No. AS-IA-112-M05) and the National Science and Technology Council, Taiwan (111-2112-M-001-085-MY3). The authors thank the National Center for High-performance Computing (NCHC) for providing computational and storage resources. C.-H.H. and Y.-C.C. acknowledged the support from the Partnership Program for the Connection to the Top Labs in the World - Dragon Gate Program (113-2926-I-002-511-G) and 113-2628-E-002-021-MY4. J.-C.K. and Y.-C.L. acknowledge the support of NSTC grant (113-2221-E-A49-012-MY3). M.-C. W. and V.T. express gratitude for the financial support provided by Chang Gung University (URRPD2Q0041). We greatly appreciate the fruitful discussion and technical support from Kosuke Nagashio and Atsuo Yamada.

Author contributions:

C.-C.T., J.-H.F., and V.T. conceived the study. C.-C.T., C.-H.H., and S.R.C. performed the experiments and analyzed the data. J.-C.K., Y.-C.L., and C.-W.P. performed the DFT and PES calculations. A.L., R.I., and N.S. performed the HR-STEM characterizations. C.-C.T. conducted the STS/M. C.L. established the CVD setup. W.-C.C., M.C.W., and F.-Z.C. deposited HfO_2 dielectric. Y.L.H. and C.-Z.D. designed the electrode patterns and analyzed the transfer and output characteristics of BCN FETs. C.-C.T., C.-H.H., Y.-C.C., J.-C.K., C.-W.P., J.-H.F., and V.T. wrote the manuscript. All the authors discussed the results and contributed to the final version of this manuscript.

Competing interests:

The authors declare no competing interests.

Data availability:

The data from this study are available from the corresponding author on reasonable request.

References

1. Liu, Y. *et al.* Promises and prospects of two-dimensional transistors. *Nature* **591**, 43–53 (2021).
2. Rhodes, D., Chae, S. H., Ribeiro-Palau, R. & Hone, J. Disorder in van der Waals heterostructures of 2D materials. *Nat Mater* **18**, 541–549 (2019).
3. Das, S. *et al.* Transistors based on two-dimensional materials for future integrated circuits. *Nat Electron* **4**, 786–799 (2021).
4. Fu, J.-H., Chen, D.-C., Wu, Y.-J. & Tung, V. Constructing Two-Dimensional, Ordered Networks of Carbon–Carbon Bonds with Precision. *Precision Chemistry* **3**, 3–9 (2025).
5. Choi, S. H. *et al.* Large-scale synthesis of graphene and other 2D materials towards industrialization. *Nat Commun* **13**, 1484 (2022).
6. Wang, Y. *et al.* P-type electrical contacts for 2D transition-metal dichalcogenides. *Nature* **610**, 61–66 (2022).
7. Kim, K. S. *et al.* The future of two-dimensional semiconductors beyond Moore's law. *Nat Nanotechnol* **19**, 895–906 (2024).
8. Kim, K. S. *et al.* Growth-based monolithic 3D integration of single-crystal 2D semiconductors. *Nature* **636**, 615–621 (2024).
9. Kim, K. S. *et al.* Non-epitaxial single-crystal 2D material growth by geometric confinement. *Nature* **614**, 88–94 (2023).
10. Zhao, B. *et al.* Gate-driven band modulation hyperdoping for high-performance p-type 2D semiconductor transistors. *Science* **388**, 1183–1188 (2025).
11. Wang, H. *et al.* Seeded growth of single-crystal black phosphorus nanoribbons. *Nat Mater* **23**, 470–478 (2024).
12. Ci, L. *et al.* Atomic layers of hybridized boron nitride and graphene domains. *Nat Mater* **9**, 430–435 (2010).
13. Xiong, Y. *et al.* Vapour–liquid–solid–solid growth of two-dimensional non-layered β-Bi_2O_3 crystals with high hole mobility. *Nat Mater* **24**, 688–697 (2025).
14. Liu, A. *et al.* Selenium-alloyed tellurium oxide for amorphous p-channel transistors. *Nature* **629**, 798–802 (2024).
15. Ghosh, S. *et al.* A complementary two-dimensional material-based one instruction set computer. *Nature* **642**, 327–335 (2025).
16. Chen, T.-A. *et al.* Wafer-scale single-crystal hexagonal boron nitride monolayers on Cu (111). *Nature* **579**, 219–223 (2020).
17. Ma, K. Y. *et al.* Epitaxial single-crystal hexagonal boron nitride multilayers on Ni (111). *Nature* **606**, 88–93 (2022).

18. Fukamachi, S. *et al.* Large-area synthesis and transfer of multilayer hexagonal boron nitride for enhanced graphene device arrays. *Nat Electron* **6**, 126–136 (2023).
19. Kong, W. *et al.* Path towards graphene commercialization from lab to market. *Nat Nanotechnol* **14**, 927–938 (2019).
20. Novoselov, K. S. *et al.* Electric Field Effect in Atomically Thin Carbon Films. *Science (1979)* **306**, 666–669 (2004).
21. Kaner, R. B., Kouvetakis, J., Warble, C. E., Sattler, M. L. & Bartlett, N. Boron-carbon-nitrogen materials of graphite-like structure. *Mater Res Bull* **22**, 399–404 (1987).
22. Mendelson, N. *et al.* Identifying carbon as the source of visible single-photon emission from hexagonal boron nitride. *Nat Mater* **20**, 321–328 (2021).
23. Weng-Sieh, Z. *et al.* Synthesis of $B_xC_yN_z$ nanotubules. *Phys Rev B* **51**, 11229–11232 (1995).
24. Kang, K. *et al.* High-mobility three-atom-thick semiconducting films with wafer-scale homogeneity. *Nature* **520**, 656–660 (2015).
25. Fu, J.-H. *et al.* Oriented lateral growth of two-dimensional materials on c-plane sapphire. *Nat Nanotechnol* **18**, 1289–1294 (2023).
26. Stephan, O. *et al.* Doping Graphitic and Carbon Nanotube Structures with Boron and Nitrogen. *Science (1979)* **266**, 1683–1685 (1994).
27. Kouvetakis, J. *et al.* Novel aspects of graphite intercalation by fluorine and fluorides and new B/C, C/N and B/C/N materials based on the graphite network. *Synth Met* **34**, 1–7 (1989).
28. Watanabe, M. O., Itoh, S., Mizushima, K. & Sasaki, T. Bonding characterization of BC_2N thin films. *Appl Phys Lett* **68**, 2962–2964 (1996).
29. Pimenta, M. A. *et al.* Studying disorder in graphite-based systems by Raman spectroscopy. *Phys. Chem. Chem. Phys.* **9**, 1276–1290 (2007).
30. Chen, P.-J. *et al.* Visualizing Local Superconductivity of NbTiN Nanowires to Probe Inhomogeneity in Single-Photon Detectors. *ACS Applied Optical Materials* **2**, 68–75 (2024).
31. Chou, S.-A. *et al.* Large-scale alkali-assisted growth of monolayer and bilayer WSe_2 with a low defect density. *Nat Commun* **16**, 2777 (2025).
32. Kwon, G. *et al.* Interaction- and defect-free van der Waals contacts between metals and two-dimensional semiconductors. *Nat Electron* **5**, 241–247 (2022).
33. Zhu, H. *et al.* Step engineering for nucleation and domain orientation control in WSe_2 epitaxy on c-plane sapphire. *Nat Nanotechnol* **18**, 1295–1302 (2023).
34. Zhang, B. Y. *et al.* Hexagonal metal oxide monolayers derived from the metal–gas interface. *Nat Mater* **20**, 1073–1078 (2021).

Figures

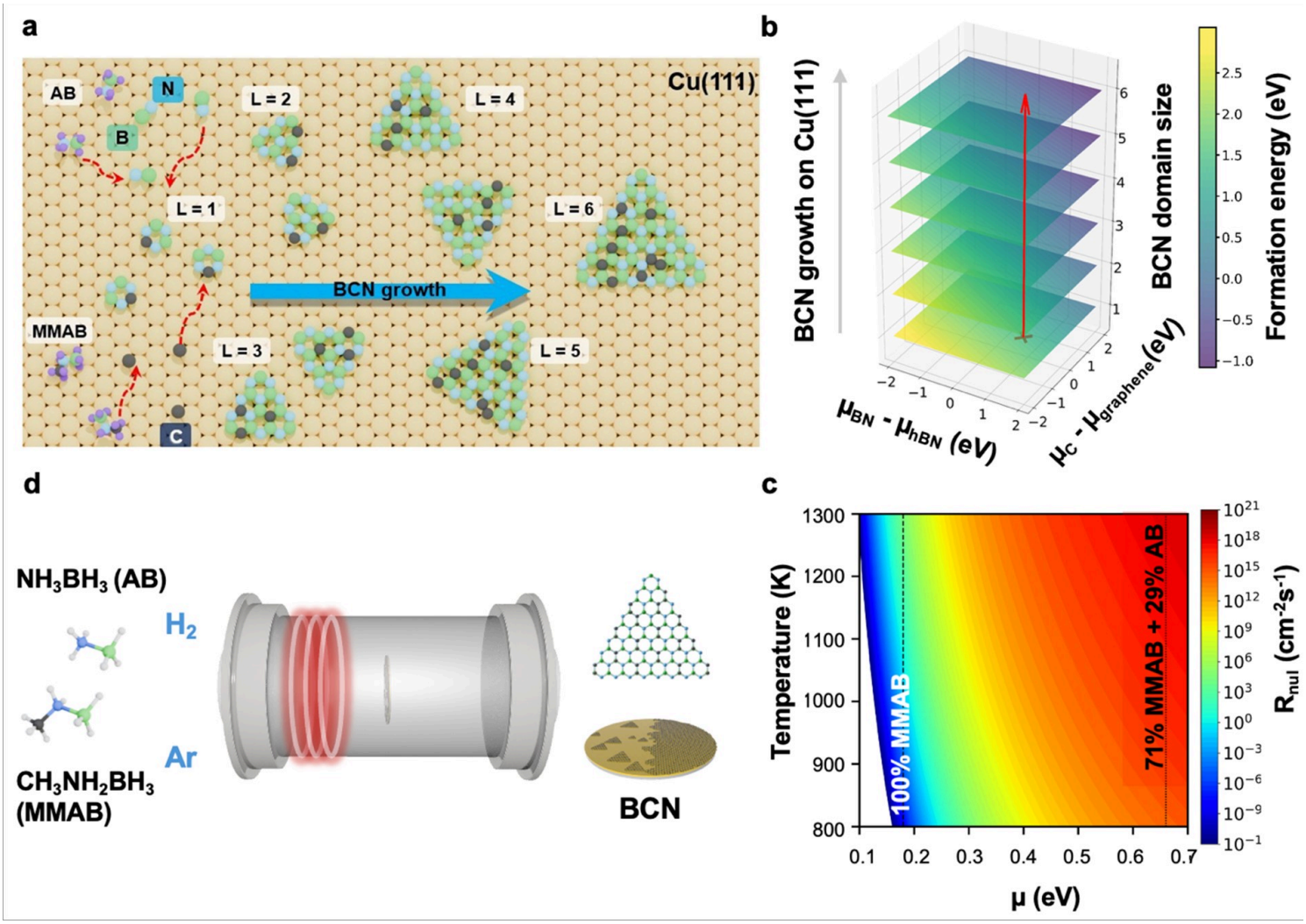


Figure 1

Simulation and wafer-scale synthesis of BCN. a, Two-dimensional (2D) potential energy surface (PES) simulation results shed light on the possible reaction pathways on Cu (111), where adsorption of *C and subsequent coupling with *B-N into BCN are thermodynamically favored. **b,** PES as a function of nucleating BCN flakes of varying sizes (L = 1-6). Lateral growth of BCN flakes becomes energetically favorable (stabilized) as opposed to the chemical potential of h-BN and graphene, respectively. **c,** 2D nucleation rate map further underscores the drastic difference in nucleation rates (~10^{15} $cm^{-2}s^{-1}$) when employing the binary precursors of ammonia borane (AB) and monomethyl ammonia borane (MMAB). **d,** Schematic illustration of our customized chemical vapor deposition (CVD) setup. AB and MMAB are individually introduced to the growth setup with individual mass flow controllers (MFCs).

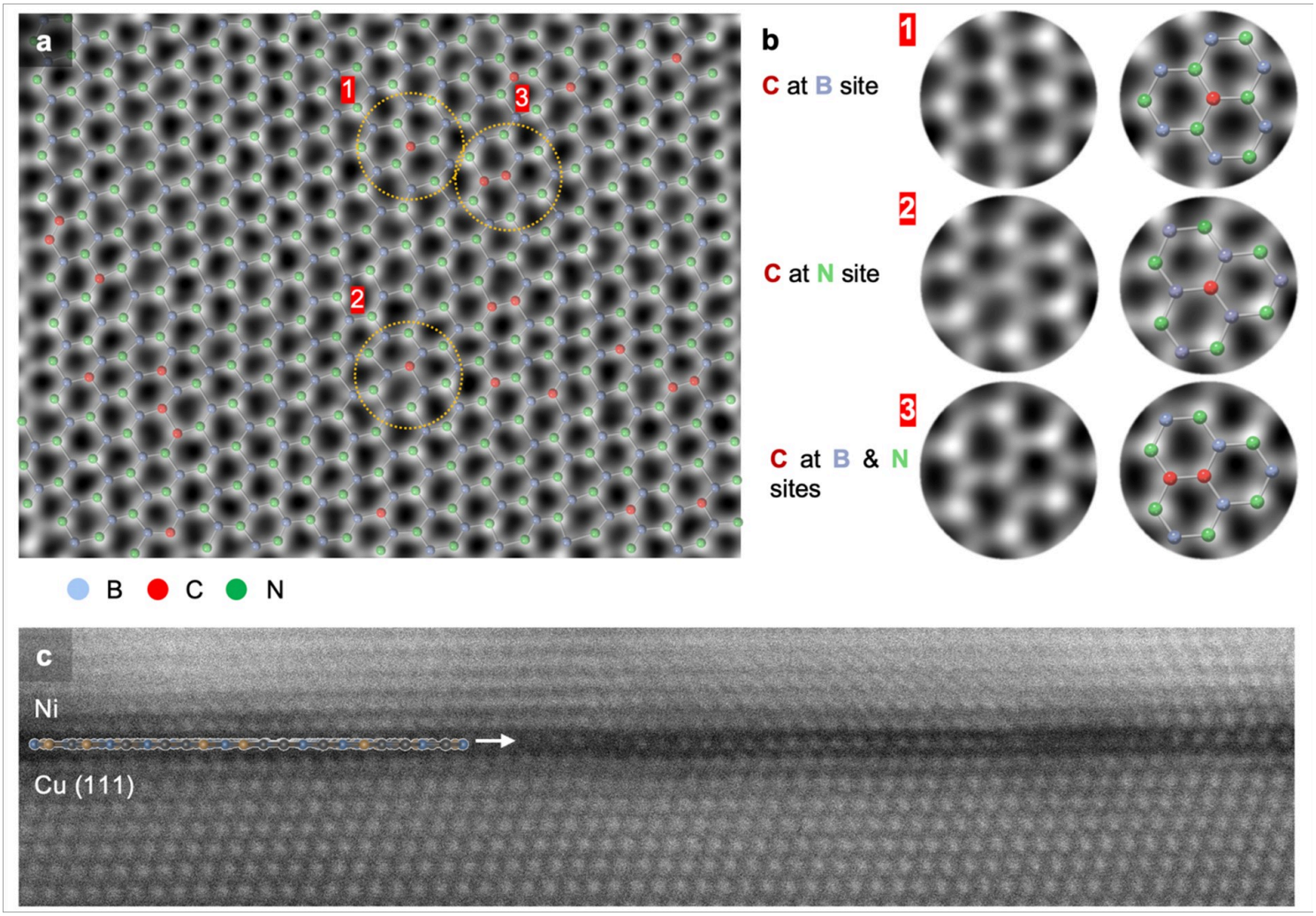


Figure 2

Atomically resolved HR-STEM images of Monolayer BCN film. a, An HR-STEM image of monolayer (ML) BCN film. The exact coordination environment of each atom can be resolved. Atom-by-atom analyses reveal that 16 carbon atoms, both atomically substituted form and dimers, are found at the N site, while 9 are found at the B site, as indicated in areas 1, 2, and 3. Note that, despite the long-range order and uniformity, the hexagonal lattices are locally distorted, closely resembling the strained silicon (Si). **b,** Atomically substituted carbon and dimer are the prevailing forms of doping within the continuously crystallized but locally distorted BN lattices. **c,**Cross-sectional HR-STEM image indicates that the as-grown BCN is one atomic layer thick.

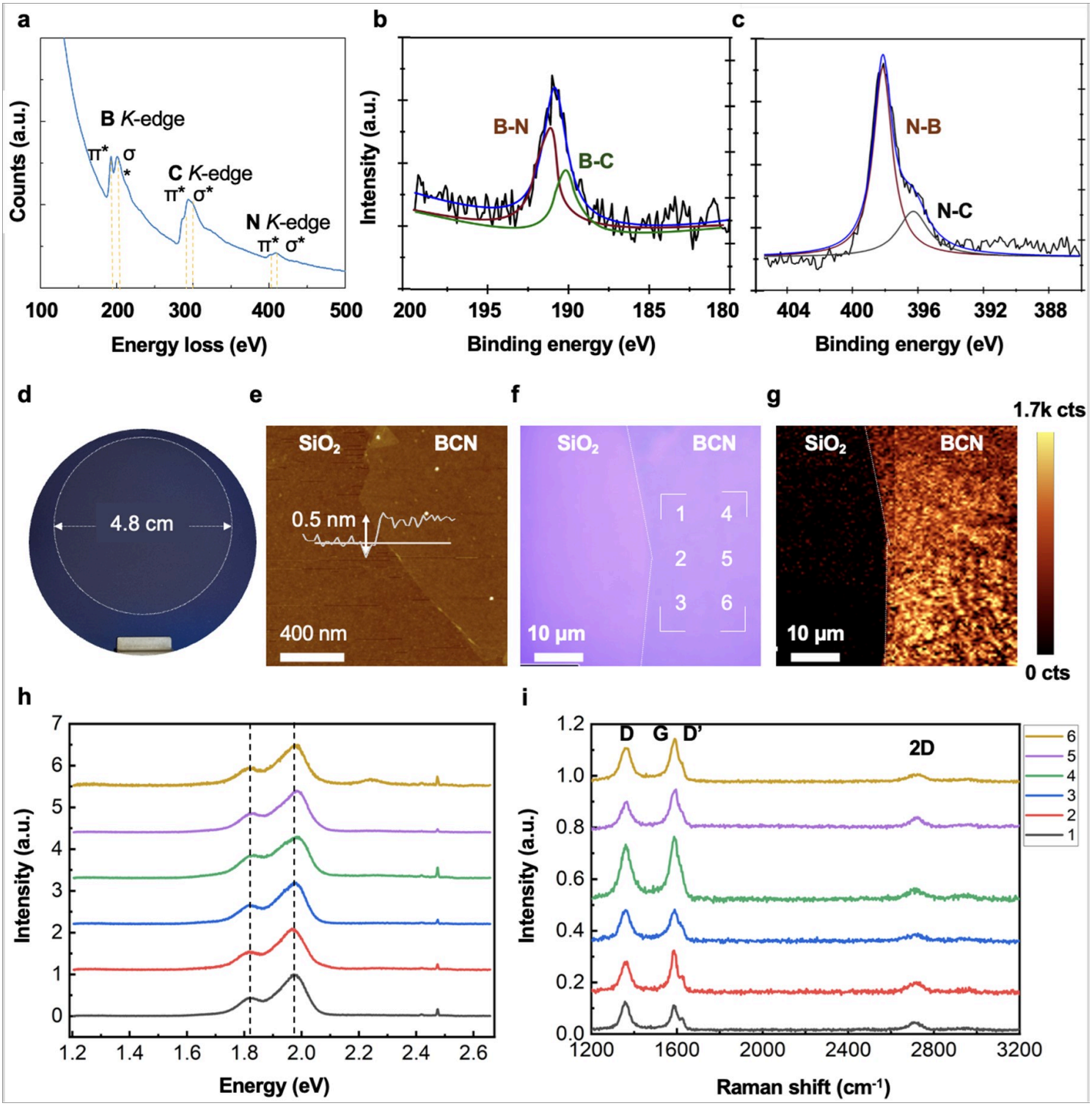


Figure 3

Multi-scale characterizations of BCN. a, K-shell excitations of B, C, and N are revealed from the core EELS spectra taken from monolayer BCN films. XPS spectra of the **b,** B and **c,** N 1s core levels, in tandem with deconvoluted curves obtained by Gaussian fitting, suggest multi-bonding environments, confirming the substitution of B and N by C. **d,** A photograph shows the integrity of a monolayer BCN film transferred from the growth substrate to Si/SiO_2 substrate. **e,** Line scan from AFM determines the step height from the edge of BCN to the supported Si/SiO_2 substrate (step height of ~ 0.5 nm). **f,** Optical

microscope (OM) image, and **g,** the corresponding PL mapping at 1.85 eV, collectively attest to the spatial uniformity. **h,** PL and **i,** Raman spectra taken at the six marked positions on the ML BCN film on SiO_2 (300 nm).

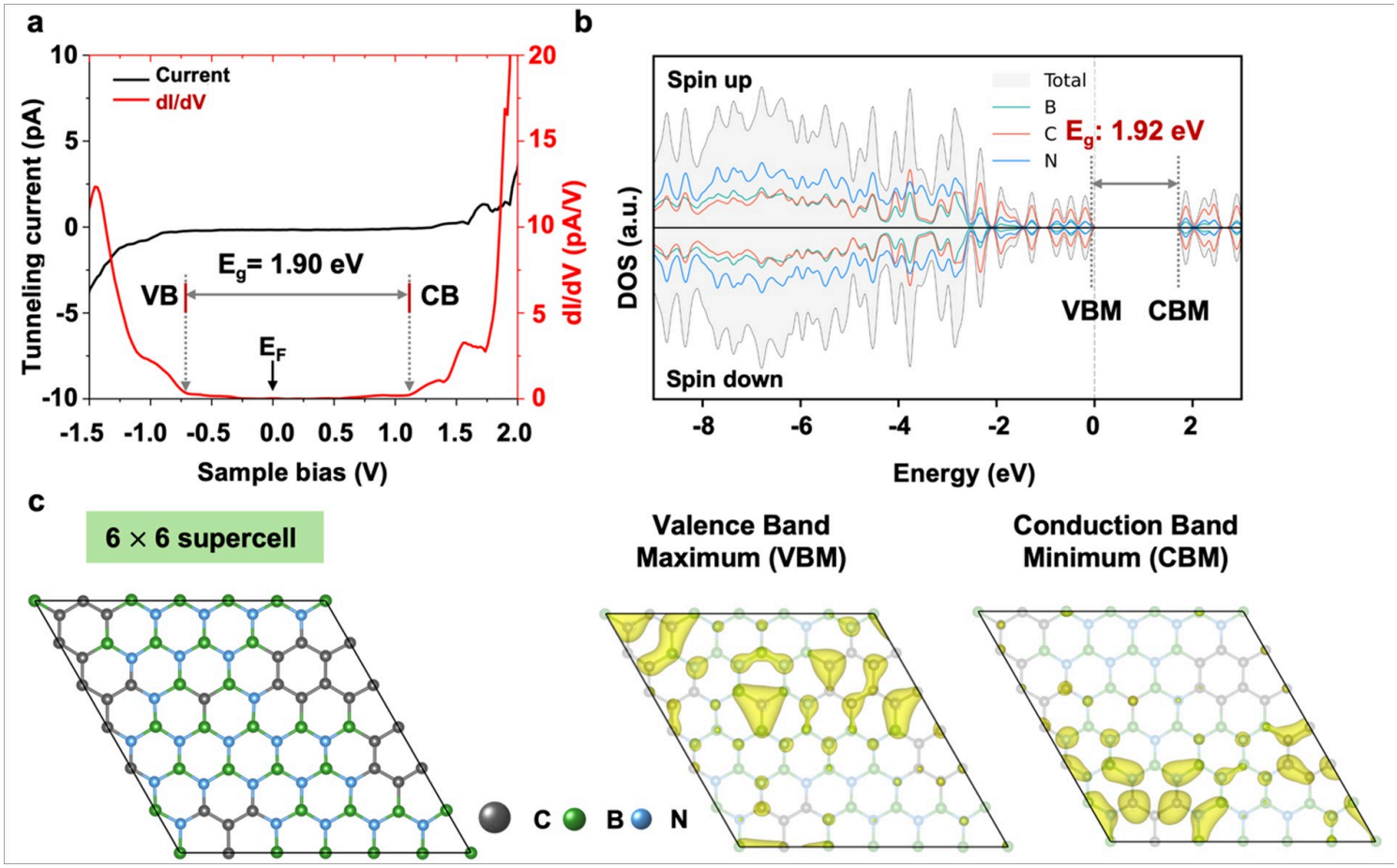


Figure 4

Electronic structure and band gap. a, Scanning tunneling microscopy and spectroscopy (STM/S) measurements determine the bandgap of an ML BCN on Cu (111), resulting in a value of ~1.90 eV. The Fermi level is aligned to 0 eV. **b,** Density of states (DOS) of the ML BCN model supports the experimental observation, indicating a bandgap of ~1.92 eV. **c,** Partial charge density plots of the valence band maximum (VBM) and conduction band minimum (CBM) show the spatial distribution of the delocalized charge density. The isosurface value of the partial charge density is set to 0.001 e/Br^3.

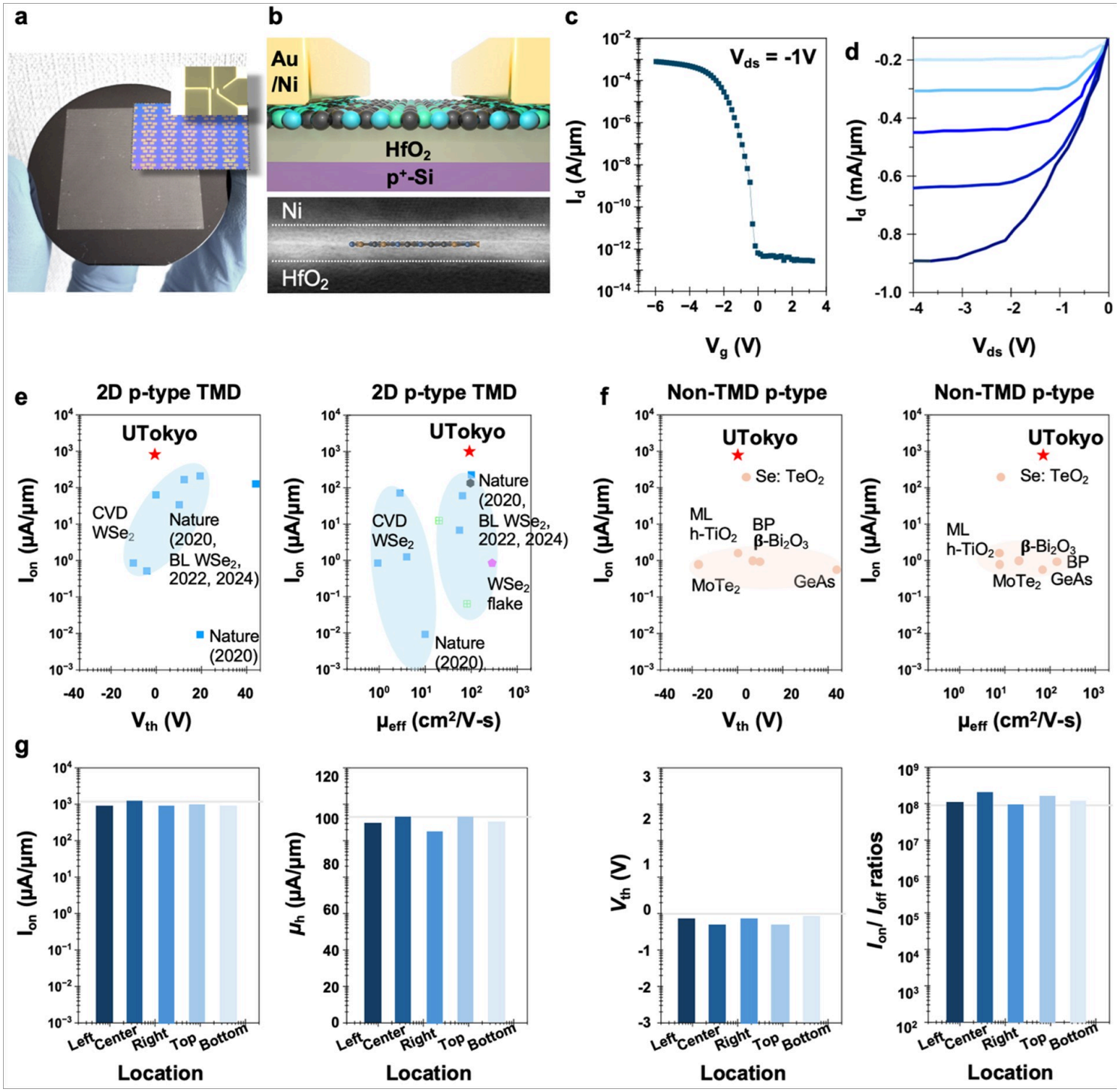


Figure 5

Electrical characterization of p-channel BCN FETs on a 20 nm HfO_2. a, Photograph of BCN FET arrays on a 2-inch HfO_2/Si wafer. The inset shows micrographs of an individual FET and FET arrays. Bright field (BF) cross-sectional HRTEM confirms the monolayer BCN and van der Waals (vdW) gaps between HfO_2 and Ni. **b,** Schematic illustration shows the BCN FET geometry and the corresponding cross-sectional HRTEM image. **c,** Transfer characteristics of BCN FETs at V_{ds} = -1V, where L_{ch} (channel length) is 1 μm. Obtained results exhibit a maximum on-current density (I_{on}) of up to 0.9 mA/μm, threshold voltage (V_{th})

of -0.45 V, a field-effect mobility (μ_h) of up to 100 cm^2/V-s, and an on/off ratio of 10^8. **d,** Output characteristics of a BCN FET. **e,** Benchmark of I_{on} vs. μ_h and I_{on} vs. V_{th} of reported 2D TMD p-channel FETs. **f,** We further compare I_{on} vs. μ_h and I_{on} vs. V_{th} of the non-TMD p-channel FETs. **g,** Statistical distribution for I_{on}, μ_h, V_{th}, and I_{on}/I_{off} ratios measured at different locations on a 2-inch wafer. Note that dotted lines indicate the requirements for meeting the 2028 International Roadmap for Devices and Systems challenge for core logic devices

Supplementary Files

This is a list of supplementary files associated with this preprint. Click to download.

- BCNManuscriptSI.docx